



# Hyper-EMG: A new probability distribution function composed of Exponentially Modified Gaussian distributions to analyze asymmetric peak shapes in high-resolution time-of-flight mass spectrometry

S. Purushothaman <sup>a,\*</sup>, S. Ayet San Andrés <sup>a,b</sup>, J. Bergmann <sup>b</sup>, T. Dickel <sup>a,b</sup>, J. Ebert <sup>b</sup>, H. Geissel <sup>a,b</sup>, C. Hornung <sup>b</sup>, W.R. Plaß <sup>a,b</sup>, C. Rappold <sup>a,b</sup>, C. Scheidenberger <sup>a,b</sup>, Y.K. Tanaka <sup>a,b</sup>, M.I. Yavor <sup>c</sup>

<sup>a</sup> GSI Helmholtzzentrum für Schwerionenforschung, 64291 Darmstadt, Germany

<sup>b</sup> Justus-Liebig Universität Gießen, 35392 Gießen, Germany

<sup>c</sup> Institute for Analytical Instrumentation, Russian Academy of Sciences, 190103 St. Petersburg, Russia



## ARTICLE INFO

### Article history:

Received 31 December 2016

Received in revised form 15 July 2017

Accepted 21 July 2017

Available online 29 July 2017

### Keywords:

Analysis of asymmetric peak shapes  
Mass and abundance determination  
Hyper-Exponentially Modified Gaussian  
Exponentially Modified Gaussian  
Mixture distributions  
High-resolution mass spectrometry  
Multiple-reflection time-of-flight mass spectrometer

## ABSTRACT

A new probability distribution function (PDF) called hyper-Exponentially Modified Gaussian (hyper-EMG) is introduced for the analysis of high-resolution spectra from multiple-reflection time-of-flight mass spectrometers. The hyper-EMG consists of a central Gaussian distribution modified by multiple exponential tails with different strengths at one or both sides. The basic statistical properties of the new PDF are given and the analysis of mass spectra containing separated and overlapping peaks is presented. The main requirement is to accurately determine the positions and areas of the individual mass peaks. From the distances of positions the mass values can be determined, from the areas the population of different ground and isomeric states can be obtained. The hyper-EMG has been applied to high-resolution time and mass spectra characterized by mass resolving powers of 140,000 and 520,000 obtained with  $^{133}\text{Cs}^+$  and  $^{39}\text{K}^+$  ions, respectively. From the measured mass distribution of  $^{39}\text{K}^+$  ions, an overlapping distribution of two peaks with an area ratio of 1:10 and a mass difference of 2.6 ppm (parts-per-million) is generated and analyzed. The results reveal significant advantages of the new PDF for the evaluation of overlapping distributions for accurate mass and area determinations compared with commonly used PDFs which are more than one order of magnitude less accurate. It is obvious that the hyper-EMG can be favorably applied also to other fields.

© 2017 Elsevier B.V. All rights reserved.

## 1. Introduction

The investigation of short-lived exotic nuclei is a major research field in many modern accelerator laboratories worldwide [1]. Exotic nuclei, characterized by extreme proton-to-neutron ratios compared to stable nuclides, reveal novel features of the nuclear force. Therefore, the measured properties of exotic nuclei can contribute to improve substantially the understanding of the strong interaction and the synthesis of the elements in the universe [2]. High-resolution accurate mass measurements of exotic nuclei reflect the nuclear binding energy which determines the structure and stability of the measured species.

New key experimental tools in this field are multiple-reflection time-of-flight mass spectrometers (MR-TOF-MS) tailored to measure the mass and abundance of exotic nuclides [3–7]. The ground-state mass of a nucleus is a basic property. However, in some investigations the masses of excited states are also of high interest in nuclear spectroscopy and reaction studies. The lifetime of the excited (isomeric) states [8] can have a large range, e.g., from nanoseconds to many years. Depending on the excitation energy and the resolution of the spectrometer the two mass populations can overlap and must be disentangled for at least two reasons: firstly to assign unambiguously the value of the ground-state mass and secondly to deduce in addition the population of the isomeric state and the excitation energy. From these requirements, it is obvious that the positions and the areas of the observed overlapping distributions must be accurately determined.

In MR-TOF mass spectrometry the measured time distributions are converted into mass distributions and the corresponding

\* Corresponding author.

E-mail address: [S.Purushothaman@gsi.de](mailto:S.Purushothaman@gsi.de) (S. Purushothaman).

areas can yield abundances of isotopes, reaction probabilities for their production and finally also the population of the observed ground and excited states. A critical part of the analysis of the spectrum is the exact reproduction of the shape of the measured peaks. Often these peaks can be simply described by pure Gaussian functions, particularly when statistical processes dominate the probability distribution. However, in high-resolution measurements, where the phase-space of the trapped ions has been strongly reduced by experimental methods, the contributions of image aberrations, field imperfections (contributions of higher-multipole components) and mechanical misalignments are clearly observed in the tails of the distribution and thus require non-Gaussian analysis methods.

In the literature, a wide range of probability distribution function (PDFs) are proposed to analyze non-Gaussian distributions [9–20]. The properties of the previous often-used PDFs are summarized in the first part of this paper and compared with the herein proposed new PDF, the hyper-EMG.

The hyper-Exponentially Modified Gaussian (hyper-EMG) proves superior in the analysis of a spectra measured with a MR-TOF-MS. Measured high-resolution time and mass spectra are analyzed with previously applied PDFs and the new hyper-EMG. The comparison clearly demonstrates the power and versatility of the hyper-EMG.

## 2. Commonly used skewed non-Gaussian functions

The so-called Exponentially Modified Gaussian (EMG) function is a widely-used function to model the peak shape with exponential deviations in the tails of the central Gaussian. An EMG is obtained by the convolution of a Gaussian and a truncated exponential function. Two types of EMG appear in the literature depending on the asymmetry of the peak shape. They are characterized by a positive skew or a negative skew, i.e., they have exponential tails in the positive and/or negative directions. However, in the literature the term EMG is used for both positively and negatively skewed EMGs. For the sake of clarity, in this article the terms Positively Skewed Exponentially Modified Gaussian (PS-EMG) and Negatively Skewed Exponentially Modified Gaussian (NS-EMG) are used to make the distinction.

An EMG PDF describes the distribution of the sum of two independent random variables, one being exponentially and the other Gaussian distributed. Since the joint PDF of the sum of two independent continuous random variables is given by the convolution of their PDFs [21,22], the EMG PDF is obtained by the convolution of the PDFs of a Gaussian distribution and an exponential distribution. A convolution is indicated by the symbol \* in this work.

The PDF  $f_G(x; \sigma_G, \mu_G)$  of a Gaussian distribution with a mean value  $\mu_G$  and a variance  $\sigma_G^2$  ( $\sigma_G > 0$ ) is defined as:

$$f_G(x; \mu_G, \sigma_G) = \frac{1}{\sqrt{2\pi\sigma_G^2}} \exp\left[-\frac{(x - \mu_G)^2}{2\sigma_G^2}\right], \quad (1)$$

The exponential distribution defined for the positive arguments is characterized by the PDF  $f_{+e}(x; \tau_+)$ :

$$f_{+e}(x; \tau_+) = \begin{cases} \frac{1}{\tau_+} \exp\left[-\frac{x}{\tau_+}\right] & \text{if } x \geq 0 \\ 0 & \text{if } x < 0, \end{cases} \quad (2)$$

where  $\tau_+ > 0$  is the scale parameter or standard deviation of the exponential distribution. In what follows, the Gaussian PDF  $f_G(x; \sigma_G, \mu_G)$  and the exponential PDF  $f_{+e}(x; \tau_+)$  are written as  $f_G(x)$  and  $f_{+e}(x)$ , respectively. The support of  $f_{+e}(x)$  is the set of positive real numbers. The joint PDF  $f_{+emg}(x; \sigma_G, \mu_G, \tau_+)$  of a Gaussian distribution and an

exponential distribution defined for the positive arguments is given by:

$$\begin{aligned} f_{+emg}(x) &= f_{+e}(x) * f_G(x) = \int_{-\infty}^{+\infty} f_{+e}(u) f_G(x-u) du \\ &= \frac{1}{\tau_+ \sqrt{2\pi\sigma_G^2}} \int_0^{+\infty} \exp\left[-\frac{u}{\tau_+}\right] \exp\left[-\frac{(x-u-\mu_G)^2}{2\sigma_G^2}\right] du \\ &= \frac{1}{2\tau_+} \exp\left[\left(\frac{\sigma_G}{\sqrt{2}\tau_+}\right)^2 - \frac{(x-\mu_G)}{\tau_+}\right] \\ &\quad \operatorname{erfc}\left[\frac{\sigma_G}{\sqrt{2}\tau_+} - \frac{(x-\mu_G)}{\sqrt{2}\sigma_G}\right], \end{aligned} \quad (3)$$

$f_{+emg}(x)$  is generally known as EMG distribution but because of its characteristic positive skew it will be referred to as PS-EMG in what follows.

Similarly a NS-EMG  $f_{-emg}(x; \sigma_G, \mu_G, \tau_-)$  can be obtained by the convolution of a Gaussian distribution  $f_G(x)$  and an exponential distribution defined for the negative arguments, which is characterized by the PDF  $f_{-e}(x; \tau_-)$ :

$$f_{-e}(x; \tau_-) = \begin{cases} 0 & \text{if } x > 0 \\ \frac{1}{\tau_-} \exp\left[\frac{x}{\tau_-}\right] & \text{if } x \leq 0, \end{cases} \quad (4)$$

where  $\tau_- > 0$  is the scale parameter or standard deviation of the distribution. The support of  $f_{-e}(x)$  is the set of negative real numbers. The PDF of a NS-EMG  $f_{-emg}(x; \sigma_G, \mu_G, \tau_-)$  is thus given by:

$$\begin{aligned} f_{-emg}(x) &= f_{-e}(x) * f_G(x) = \int_{-\infty}^{+\infty} f_{-e}(u) f_G(x-u) du \\ &= \frac{1}{\tau_- \sqrt{2\pi\sigma_G^2}} \int_{-\infty}^0 \exp\left[\frac{u}{\tau_-}\right] \exp\left[-\frac{(x-u-\mu_G)^2}{2\sigma_G^2}\right] du \\ &= \frac{1}{2\tau_-} \exp\left[\left(\frac{\sigma_G}{\sqrt{2}\tau_-}\right)^2 + \frac{(x-\mu_G)}{\tau_-}\right] \\ &\quad \operatorname{erfc}\left[\frac{\sigma_G}{\sqrt{2}\tau_-} + \frac{(x-\mu_G)}{\sqrt{2}\sigma_G}\right]. \end{aligned} \quad (5)$$

Both  $f_{-emg}(x)$  and  $f_{+emg}(x)$  are continuous, real-valued and supported on the interval  $(-\infty, +\infty)$ .

## 3. Properties of the hyper-EMG

### 3.1. Mixture distribution

Mixture distributions describe random variables that are drawn from a collection of other random variables. This scenario arises when different mechanisms generate data according to different models and the variable that indicates which mechanism generated an observation is not recorded, and only the response variable is available [23–25]. In statistics, this is a tool to model heterogeneity in the sense that different elements of a sample may belong to different components. However, it may also be simply used as an extremely flexible method of modeling to achieve a good fit to data which could not be accommodated by a single distribution. The PDF of a mixture distribution is expressed as a convex combination of arbitrary PDFs:

$$f(x; \eta_i) = \sum_{i=1}^n \eta_i f_i(x), \quad (6)$$

where  $f_1(x), \dots, f_n(x)$  is a finite set of component PDFs. Each of these PDFs reflect the behavior of an underlying process, belonging to a different mechanism and  $\eta_1, \dots, \eta_n$  are the mixing weights such that  $1 \geq \eta_i \geq 0$  and  $\sum_{i=1}^n \eta_i = 1$  and that  $f_i(x)$  are normalized.

By definition the component distributions can be of different types, for example exponential-gamma, exponential-Weibull, etc. [26]. If all the components of a mixture distribution belong to the same parametric family (e.g., all Gaussian, all exponential, etc.), it is called a parametric mixture model distribution. An example is the finite mixture of exponential distributions [27], which is often referred to as hyper-exponential distribution,  $h_{\pm e}(x; \tau_{\pm i}, \eta_{\pm i})$ . Here the + and – signs indicate if the function is defined either for positive or negative arguments, respectively. The PDF of a hyper-exponential distribution is given by the convex combination of exponential distributions  $f_{\pm e}(x; \tau_{\pm i})$  (see Eqs. (2) and (4)):

$$h_{\pm e}(x; \tau_{\pm i}, \eta_{\pm i}) = \sum_{i=1}^n \eta_{\pm i} f_{\pm e}(x; \tau_{\pm i}), \quad (7)$$

such that the parameters  $\tau_{\pm i} > 0$ ,  $1 \geq \eta_{\pm i} \geq 0$  and  $\sum_{i=1}^n \eta_{\pm i} = 1$ .

In what follows, the hyper-exponential PDF for the positive arguments  $h_{+e}(x; \tau_{+i}, \eta_{+i})$  and the hyper-exponential PDF for the negative arguments  $h_{-e}(x; \tau_{-i}, \eta_{-i})$  are written as  $h_{+e}(x)$  and  $h_{-e}(x)$ , respectively.

The PDF of a hyper-exponential distribution is thus evidently a convex combination of PDFs of exponential distributions. The support of  $h_{+e}(x)$  is the set of positive real numbers and for  $h_{-e}(x)$  it is the set of negative real numbers.

### 3.2. Hyper-EMG distribution

The PDF of a mixture distribution, whose component distributions are either all PS-EMG or NS-EMG distributions, is given by a convex combination of corresponding PDFs. This PDF can successfully model asymmetry caused by a Gaussian peak shape having

$$\begin{aligned} h_{emg}(x) &= \Theta h_{-emg}(x) + (1 - \Theta) h_{+emg}(x) \\ &= \Theta \sum_{i=1}^m \eta_{-i} f_{-emg}(x) + (1 - \Theta) \sum_{i=1}^n \eta_{+i} f_{+emg}(x) \\ &= \Theta \sum_{i=1}^m \frac{\eta_{-i}}{2\tau_{-i}} \exp \left[ \left( \frac{\sigma_G}{\sqrt{2}\tau_{-i}} \right)^2 + \frac{(x - \mu_G)}{\tau_{-i}} \right] \operatorname{erfc} \left[ \frac{\sigma_G}{\sqrt{2}\tau_{-i}} + \frac{(x - \mu_G)}{\sqrt{2}\sigma_G} \right] \\ &\quad + (1 - \Theta) \sum_{i=1}^n \frac{\eta_{+i}}{2\tau_{+i}} \exp \left[ \left( \frac{\sigma_G}{\sqrt{2}\tau_{+i}} \right)^2 - \frac{(x - \mu_G)}{\tau_{+i}} \right] \operatorname{erfc} \left[ \frac{\sigma_G}{\sqrt{2}\tau_{+i}} - \frac{(x - \mu_G)}{\sqrt{2}\sigma_G} \right], \end{aligned} \quad (10)$$

---

multiple exponential tailings with different strengths towards one of its sides. Tailing will cause a shift in the maximum of the peak shape and introduces a positive or negative skew in the peak shape that depends on the tailing direction.

The PDF  $h_{+emg}(x; \sigma_G, \mu_G, \tau_{+i}, \eta_{+i})$  of the mixture distribution of PS-EMGs is given by the joint PDF of a hyper-exponential distribution (defined for the positive arguments)  $h_{+e}(x)$  (see Eq. (7)) and a Gaussian distribution  $f_G(x)$  (see Eq. (1)):

$$\begin{aligned} h_{+emg}(x; \sigma_G, \mu_G, \tau_{+i}, \eta_{+i}) &= h_{+e}(x) * f_G(x) \\ &= \sum_{i=1}^n \eta_{+i} f_{+e}(x) * f_G(x) \\ &= \sum_{i=1}^n \eta_{+i} f_{+emg}(x), \end{aligned} \quad (8)$$

which is a convex combination of PS-EMG PDFs (see Eq. (3)). This function is referred to as Positive Skewed hyper-EMG (PS-hyper-EMG) in what follows (see Fig. 1b).

Similarly the PDF of the mixture distribution of NS-EMGs,  $h_{-emg}(x; \sigma_G, \mu_G, \tau_{-i}, \eta_{-i})$  can be expressed as a convex combination of NS-EMG PDFs (see Eq. (5)):

$$h_{-emg}(x; \sigma_G, \mu_G, \tau_{-i}, \eta_{-i}) = \sum_{i=1}^n \eta_{-i} f_{-emg}(x). \quad (9)$$

This PDF is referred to as Negative Skewed hyper-EMG (NS-hyper-EMG) in what follows (see Fig. 1a).

Both  $h_{-emg}(x)$  and  $h_{+emg}(x)$  are continuous, real-valued and supported on the interval  $(-\infty, +\infty)$ . The peak maximum of these distributions are always on or within half of the unmodified Gaussian towards the tailing direction. In a wide range of fields the recorded experimental data are often dominated by statistical processes and only slightly deviate from a Gaussian profile because of symmetric or asymmetric (exponential like) tailings on both of its ends. The resulting peak shape can be either symmetric or asymmetric but deviates significantly from Gaussian to a hyper-exponential form at regions far from the peak maximum.

The new PDF which is capable of accommodating this functional behavior is developed from the basic statistical principles and is presented in the following. The deviation from a pure Gaussian function is due to the multiple exponential tailings of different strengths on both of its tails. It can be described by using the PDF of a two component mixture distribution of a PS-hyper-EMG and a NS-hyper-EMG. The skewness of this function can be either positive, negative or zero depending on the strength, direction and scale parameters of constituting exponential tails. Such a PDF will be referred to as hyper-EMG distribution in what follows.

A hyper-EMG PDF  $h_{emg}(x; \sigma_G, \mu_G, \tau_{+i}, \tau_{-i}, \eta_{+i}, \eta_{-i}, \Theta)$  is given by a convex combination of PDFs of a PS-hyper-EMG distribution and a NS-hyper-EMG distribution (see Eqs. (8) and (9)) with the mixing weight  $\Theta$  (see Fig. 1c). It is expressed as:

$$h_{emg}(x) = (\Theta h_{-e}(x; \tau_{-i}) + (1 - \Theta) h_{+e}(x; \tau_{+i})) * f_G(x) \quad (11)$$

Such that  $1 \geq \Theta \geq 0$ ,  $\sigma_G > 0$  and  $\tau_{\pm i} > 0$ ,  $\sum_{i=1}^m \eta_{-i} = 1$  and  $\sum_{i=1}^n \eta_{+i} = 1$  where  $1 \geq \eta_{\pm i} \geq 0$ .  $h_{emg}(x)$  is thus a PDF of a mixture distribution whose individual components are joint PDF of Gaussian and exponential distributions. By using the distributive property of the convolution,  $h_{emg}(x)$  can be also written as

$$h_{emg}(x) = (\Theta h_{-e}(x; \tau_{-i}) + (1 - \Theta) h_{+e}(x; \tau_{+i})) * f_G(x) \quad (11)$$

which means that the  $h_{emg}(x)$  is formed by the convolution of the PDF of a Gaussian distribution with the weighted sums of PDFs of hyper-exponential distributions defined for positive and negative arguments.  $h_{emg}(x)$  is continuous, real-valued and supported on the interval  $(-\infty, +\infty)$ .

The hyper-EMG provides a powerful tool to model the symmetric and asymmetric spreading of a Gaussian signal caused by independent processes with the individual scale parameters  $\tau$  and the strength or height of the tailing is addressed by the weight parameters  $\eta$ . The parameter  $\Theta$  addresses the relative strength of the tailings towards the negative and positive directions. A hyper-EMG PDF requires  $2N+1$  parameters to model a Gaussian distribution modified by  $N$  exponential tails. Even for the same shape parameters ( $\tau_i$ ,  $\sigma_G$  and  $\mu_G$ ), the peaks shapes can be sig-

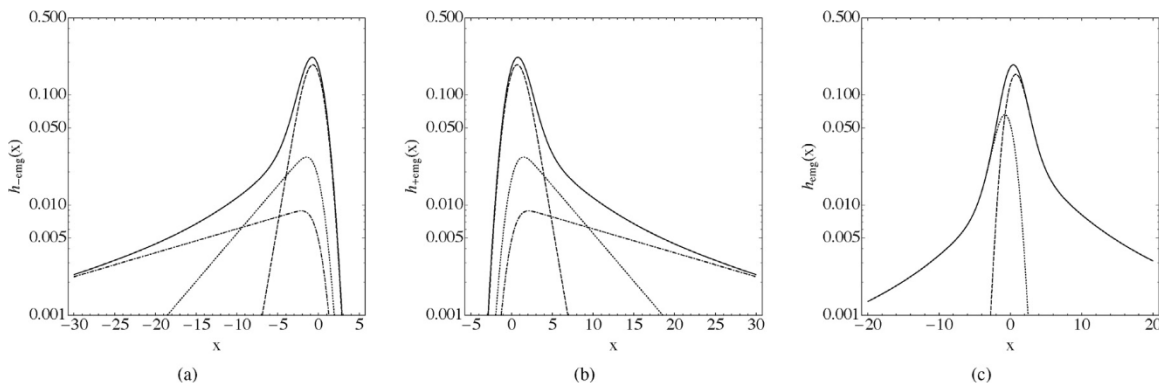


**Fig. 1.** Calculated NS-hyper-EMG, PS-hyper-EMG and the new hyper-EMG distributions. The solid lines represent the NS-hyper-EMG distribution in panel (a) and the PS-hyper-EMG distribution in panel (b) with the same shape parameters and their corresponding weighted NS-EMG and PS-EMG components. The dashed line corresponds to  $\eta_1 = 0.6$ ,  $\tau_1 = 1$ , the dotted line to  $\eta_2 = 0.2$ ,  $\tau_2 = 5$  and the dash-dotted line to  $\eta_3 = 0.2$ ,  $\tau_3 = 20$ . The solid line in panel (c) shows the hyper-EMG distribution constructed from the NS-hyper-EMG (dotted line) and PS-hyper-EMG (dashed line) distributions depicted in panel (a) and (b) with a mixing weight of  $\Theta = 0.3$ . All the distributions have the same  $\sigma_g = 1$  and  $\mu_g = 0$  values.

nificantly different for different weight parameters  $\eta_i$  and/or  $\Theta$ . PS-EMG ( $\Theta = 0$  and  $\eta_{+1} = 1$ ), NS-EMG ( $\Theta = 1$  and  $\eta_{-1} = 1$ ), PS-hyper-EMG ( $\Theta = 0$ ) and NS-hyper-EMG ( $\Theta = 1$ ) are special cases of a hyper-EMG function. The peak maximum of a hyper-EMG distribution will be always on, or within the unmodified Gaussian distribution. When  $\sigma_G \gg \tau_i$  (for all  $\tau_{+i}$  and  $\tau_{-i}$ ), the hyper-EMG approaches a Gaussian form. The convolution of a hyper-EMG PDF  $h_{emg}(x; \sigma_G, \mu_G, \tau_{+i}, \tau_{-i}, \eta_{+i}, \eta_{-i}, \Theta)$  with ' $r$ ' Gaussian PDFs with individual variances  $\sigma_{Gs}^2$  and mean values  $\mu_{Gs}$  will result in another hyper-EMG PDF  $h_{emg}(x; \sigma_{Gs}, \mu_{Gs}, \tau_{+i}, \tau_{-i}, \eta_{+i}, \eta_{-i}, \Theta)$ , where  $\sigma_{Gr}^2 = \sigma_G^2 + \sum_{s=1}^r \sigma_{Gs}^2$  is the new unmodified Gaussian variance and  $\mu_{Gr} = \mu_G + \sum_{s=1}^r \mu_{Gs}$  the new unmodified Gaussian mean. All the other parameters remain the same as for the original hyper-EMG.

#### 4. Statistical moments of a hyper-EMG

For a mixture of one-dimensional (univariate) distributions  $f_1(x), \dots, f_n(x)$  with the mixing weights  $\eta_1, \dots, \eta_n$  (see Eq. (6)), the zeroth moment (area or total probability), the first moment (mean), the second central moment (variance) and the third central moment (unnormalized skewness) can be calculated using the expressions given in Table 1. Here the areas  $A_k = 1$ , the mean values  $\mu_k$ , the variances  $\sigma_k^2$  and unnormalized skewnesses  $\theta_k$  are the corresponding moments of the component distributions. The central moments can be used to characterize the shape of the distribution, independently of translation. The variance gives the measure of dispersion of a distribution about its mean value and it is by definition a non-negative quantity. The third moment (unnormalized skewness) indicates the degree of asymmetry of a distribution. Negative values for the skewness indicate that the tailing towards negative direction is long relative to positive direction and vice versa. Symmetric distributions should have a near zero skewness whereas a zero skewness does not necessarily mean a symmetric distribution since asymmetries may even out.

PS-hyper-EMG and NS-hyper-EMG distributions are mixture distributions of PS-EMG and NS-EMG distributions, respectively. Statistical moments of the component distributions are necessary to calculate the statistical moments of the mixture distributions. The statistical moments of PS-EMG and NS-EMG distributions up to the third central moment are shown in Table 2. The statistical moments for PS-hyper-EMG and PS-hyper-EMG with component weights  $\eta_i$  and exponential scale parameters  $\tau_i$  are given in Table 3.

For a hyper-EMG distribution composed of two component mixture of a PS-hyper-EMG distribution and a NS-hyper-EMG distribution with the component weights  $(1 - \Theta)$  and  $\Theta$ , the area  $A_H$ ,

the mean value  $M_H$ , the variance  $S_H$  and the unnormalized skewness  $\theta_H$  can be calculated using Tables 1 and 3 as:

$$\begin{aligned} A_H &= \Theta A_{-h} + (1 - \Theta) A_{+h} \\ M_H &= \Theta M_{-h} + (1 - \Theta) M_{+h} \\ S_H &= \Theta S_{-h} + (1 - \Theta) S_{+h} + \Theta(1 - \Theta)(M_{-h} - M_{+h})^2 \\ \theta_H &= \Theta \theta_{-h} + (1 - \Theta) \theta_{+h} \\ &\quad + 3\Theta(1 - \Theta)(M_{-h} - M_{+h})(S_{-h} - S_{+h}) \\ &\quad + [\Theta^2(1 - \Theta) - \Theta(1 - \Theta)^2](M_{-h} - M_{+h})^3. \end{aligned} \quad (12)$$

#### 5. Application of the hyper-EMG in high-resolution time-of-flight mass spectrometry

Time-of-flight mass spectrometry (TOF-MS) is characterized by fast and broadband measurements as well as high-transmission efficiency and single-ion sensitivity [30]. The basic principle of this technique is to accelerate the ions through a potential difference of known strength. The kinetic energy of all accelerated ions is approximately the same and in the keV range. Of course, it depends on the selected charge state of the ions. The motion of an ion in the electromagnetic field is determined by its mass-to-charge ratio. In this work the ions discussed are in charge state 1+ and the terms mass and mass-to-charge ratios are used synonymously. The mass-to-charge ratios of the ions are determined from the time it takes for them to reach a detector at a given distance. The mass is proportional to the square of the flight time, and the mass resolving power ( $m/\Delta m$ ) is the ratio of the total flight time ( $t$ ) and twice the width of the time distribution ( $\Delta t$ ):

$$\left( \frac{m}{\Delta m} \right) = \frac{t}{2\Delta t} \quad (13)$$

The peaks in the time-of-flight spectra are often Gaussian-like when the uncertainty in time of flight is dominated by the initial, viz. thermal, velocity spread of the ions prior to acceleration. This leads to different flight times even for otherwise identical ions. This influence can be reduced by increasing the extraction field strength, however at the expense of an increase in the energy spread of the ion population, which leads to chromatic aberrations. Hence, a compromise has to be found for the optimal mass resolving power. A solution is to extend the flight path by use of devices with multiple passes [31]. This idea lead to the development of MR-TOF-MS [32,33] which can achieve orders of magnitude higher resolving powers compared to conventional TOF-MS. In MR-TOF-MS the ions

**Table 1**

The statistical moments of mixture distributions with the mixing weights  $\eta_k$ , the component areas  $A_k=1$ , the mean values  $\mu_k$ , the variances  $\sigma_k^2$  and the unnormalized skewnesses  $\theta_k$  [23,28].

Area ( $A_M$ )	Mean ( $M_M$ )	Variance ( $S_M$ )	Unnormalized skewness ( $\theta_M$ )
$\sum_{k=1}^p \eta_k A_k = 1$	$\sum_{k=1}^p \eta_k \mu_k$	$\sum_{k=1}^p \eta_k [\sigma_k^2 + (\mu_k - M_M)^2]$	$\sum_{k=1}^p \eta_k [\theta_k + 3\sigma_k^2(\mu_k - M_M) + (\mu_k - M_M)^3]$

**Table 2**

The statistical moments of PS-EMG [29] and NS-EMG distributions. The  $\pm$  sign in the expressions for mean value ( $M$ ) and unnormalized skewness ( $\theta$ ) denote that they are different for PS-EMG and NS-EMG PDFs. The sign  $+$  should be selected for the PS-EMG and the sign  $-$  for the NS-EMG. The exponential scale parameter  $\tau$  is  $\tau_+$  for the PS-EMG and  $\tau_-$  for the NS-EMG.  $\mu_G$  and  $\sigma_G^2$  are the mean value and variance of the unmodified Gaussian distribution.

Area ( $A$ )	Mean ( $M$ )	Variance ( $S$ )	Unnormalized skewness ( $\theta$ )
1	$\mu_G \pm \tau$	$\sigma_G^2 + \tau^2$	$\pm 2\tau^3$

are reflected back and forth multiple times in an electrostatic double mirror system (analyzer), to enhance their flight path, before they are extracted to impinge on a detector. Assuming the time-of-flight errors due to initial conditions,  $\Delta t_0$ , which include in particular the turn-around time, and the time-of-flight errors in each turn in the time-of-flight analyzer due to aberrations,  $\Delta t_a$ , are independent of each other, the mass resolving power of a multiple-pass TOF-MS is given by [34]:

$$\left( \frac{m}{\Delta m} \right) = \frac{(t_0/N_a) + t_a}{2\sqrt{(\Delta t_0/N_a)^2 + (\Delta t_a)^2}}, \quad (14)$$

where  $t_0$  is the time-of-flight from the start position to the detector without any flight path extension by reflections,  $t_a$  is the time-of-flight for a single lap in the analyzer and  $N_a$  is the number of passes in the analyzer. In the case of a large number of passes,  $N_a \rightarrow \infty$ , the overall mass resolving power tends towards the ion optical resolving power  $t_a/(2\Delta t_a)$ , which can be made orders of magnitude larger than the resolving power achievable in single-pass TOF-MS. In this way the relative influence of the width of the Gaussian peak gets reduced with increasing number of laps. The higher-order ion-optical aberrations and collisional effects with the atoms in the residual gas appear as pronounced tails at both sides of the Gaussian profile.

The mass values are determined from the peak positions of the measured spectra. The task is to accurately determine the peak positions and differences, i.e., the fitted PDF must unambiguously model the measured distributions. For the investigation of the abundance of isotopes or isomers, besides the positions, the areas must be accurately determined simultaneously [6]. The peak positions should be determined with an accuracy of  $10^{-7}$  or better and the area determined in the percentage range. In the case of well-separated peaks, the evaluation is relatively easy. However, for overlapping peaks, both, the positions and the areas will be influenced by the underlying tails from the neighboring peaks.

The position and area informations are critical for high-precision measurements in nuclear physics. Therefore, it is extremely important to have an accurate model for the measured time distributions, which can handle well any symmetric or asymmetric tailings of the peak. The hyper-EMG PDF is an ideal tool which offers the necessary flexibility to take the different processes into account

which determine the experimental distribution. The hyper-EMG has been used to analyze measured characteristic time and mass spectra from the MR-TOF-MS device [34,35]. It is a powerful and universal mass spectrometer with single-ion sensitivity and high separation power. Mass resolving powers at full width at half maximum (FWHM) as high as 600,000 and a mass accuracy of  $10^{-7}$  have been achieved [34]. This makes the apparatus ideally suited for experiments with exotic nuclei characterized by a life-time larger than a few milliseconds.

First of all, this work presents the modeling of high-resolution time-of-flight spectra over 5 orders of magnitude in the intensity with different PDFs. A simple way to get the initial parameters for the hyper-EMG is illustrated. The accuracy in position and area determination is presented by shifting measured mass spectra to simulate both well-separated and overlapping distributions.

A measured good-statistics time spectrum of  $\text{Cs}^+$  ions is presented in Fig. 2 after 210 laps in the analyzer of the MR-TOF-MS [34]. In the spectrum  $6 \times 10^5$  events were accumulated. The non-Gaussians tails are clearly visible. The total flight time was  $9.9 \times 10^6$  ns and the corresponding FWHM 35 ns. Both values yield a mass resolving power of 140,000 (Eq. (13)). The peak shape shows a Gaussian-like peak with several exponential tails of different strength on its trailing and leading edge. The hyper-EMG function (see Eq. (10)) used to analyze these data is:

$$f(x) = Ah_{\text{emg}}(x; \sigma_G, \mu_G, \tau_{+i}, \tau_{-i}, \eta_{+i}, \eta_{-i}, \Theta), \quad (15)$$

where  $A$  is the area of the peak and  $i = 1, 2, 3$ , the number of exponential tails. Since the weight parameters  $\eta_i$  follow the condition  $\sum_{i=1}^3 \eta_{\pm i} = 1$ , the number of free parameters is reduced from 16 to 14. The hyper-EMG function requires  $2(N+1)$  parameters to model a peak shape with  $N$  exponential components. An example of curve fitting is shown in Fig. 2. The iterative least-squares method [37,38] is employed, where chi-square, defined in the following formula, is minimized:

$$\chi^2 = \sum_i \left( \frac{y_i - n_i}{\sigma_i} \right)^2, \quad (16)$$

Here,  $y_i$  is a predicted value by the model function  $f(x)$  and  $n_i$  is a measured value at a given point.  $\sigma_i$  is an estimate of the standard deviation for  $n_i$ , which is defined by  $\sigma_i = \sqrt{y_i}$  and determined iteratively. The method of maximum likelihood is also used to confirm treatment of the bins with poor statistics [39]. The two methods give identical results for the data presented in Fig. 2. A good agreement between the data and the fit is also reflected by the normalized residuals (Fig. 2, panel(c)). One can see that the fit describes well the data, especially also the transitions between different exponentials. Within the uncertainties even the simple non-iterative chi-square method of  $\sigma_i = \sqrt{n_i} + 1$  gives same values for  $A$ ,  $\sigma_G$ ,  $\mu_G$ , and  $\tau_{\pm 1}$  as the two other techniques. An important advantage of the hyper-EMG, compared with many of the avail-

**Table 3**

The statistical moments of PS-hyper-EMG and NS-hyper-EMG. The  $\pm$  sign in the expressions for mean value ( $M_h$ ) and unnormalized skewness ( $\theta_h$ ) denote that they are different for PS-hyper-EMG and NS-hyper-EMG PDFs.  $+$  should be selected for the PS-hyper-EMG and the sign  $-$  for the NS-hyper-EMG. For PS-hyper-EMG  $\tau_i$  and  $\eta_i$  are  $\tau_{+i}$  and  $\eta_{+i}$  and for NS-hyper-EMG they are  $\tau_{-i}$  and  $\eta_{-i}$ .

Area ( $A_h$ )	Mean ( $M_h$ )	Variance ( $S_h$ )	Unnormalized skewness ( $\theta_h$ )
$\sum_{i=1}^n \eta_i A_i = 1$	$\mu_G \pm \sum_{i=1}^n \eta_i \tau_i$	$\sigma_G^2 + \sum_{i=1}^n [\eta_i + \eta_i(1 - \eta_i)^2] \tau_i^2$	$\pm \sum_{i=1}^n [2\eta_i \tau_i^3 + (1 - \eta_i)^3 \eta_i \tau_i^3 + 3(1 - \eta_i) \eta_i \tau_i S_i]$

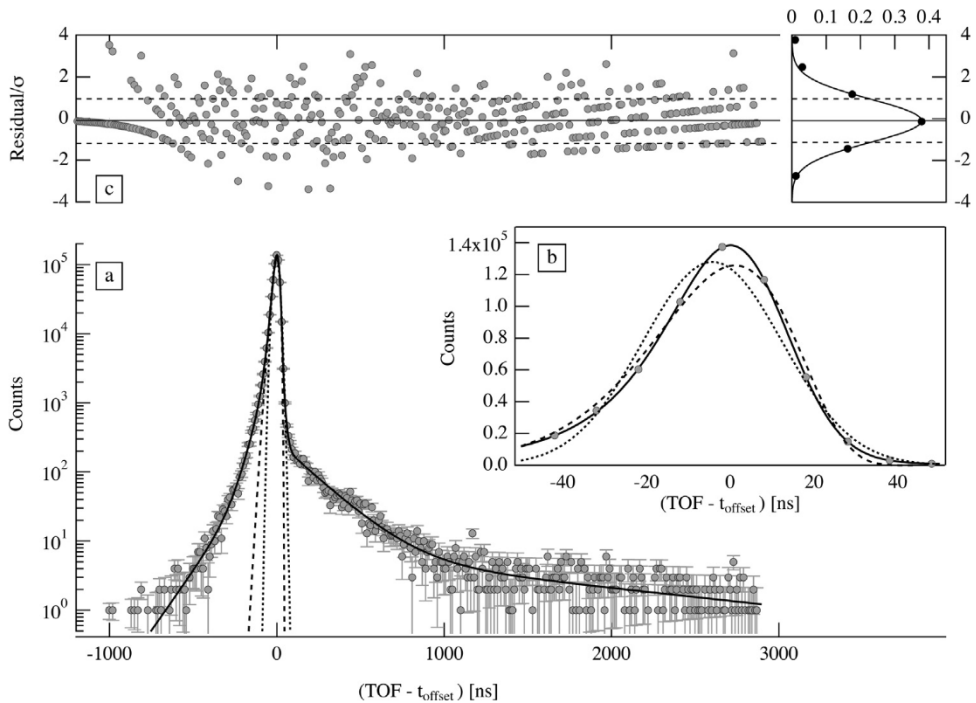


**Fig. 2.** Measured time spectrum from MR-TOF-MS [34]. The spectrum consists of  $6 \times 10^5$  events and corresponds to a total flight time of  $9.9 \times 10^6$  ns which is used as an offset in the presented spectrum. The FWHM of this time distribution is 35 ns and thus yields a mass resolving power of  $\approx 140,000$ , see Eq. (13). In panel (a), the experimental data are represented by filled gray circles. The fit with a hyper-EMG with three exponentials on the trailing and leading edges corresponds to the solid black line. The Gaussian fit and the one with the Exponential-Gaussian Hybrid function [18,36] are represented by a dotted and a dashed line, respectively. The magnified view of the distribution and the models close to the maximum of the peak are shown in panel (b). Here, the vertical axis has a linear scale. The panel (c) shows the normalized residuals from the hyper-EMG fit defined by the ratio of the residuals and the estimated standard deviations. The projection of the normalized residuals is shown on the right side.

**Table 4**

Initial guess parameters and the final parameters from the hyper-EMG fit of the distribution from Fig. 2.  $\sigma_G$  and  $\mu_G$  are the standard deviation and mean value of the unmodified Gaussian.  $\tau_-$  and  $\tau_+$  are the scale parameters of the exponential tails decaying towards negative and positive direction and  $\eta_-$  and  $\eta_+$  are corresponding weight parameters.  $A$  is the area and  $\Theta$  is the mixing weight parameter of NS-hyper-EMG and PS-hyper-EMG functions, see Eqs. (15) and (10).

Para.	Initial values	Fit parameters	
		Value	Uncertainty
$\sigma_G$	16.07 ns	10.95 ns	0.06 ns
$\mu_G$	2.25 ns	9.150 ns	0.067 ns
$\tau_{-1}$	17.4 ns	15.19 ns	0.14 ns
$\tau_{-2}$	44.9 ns	43 ns	2 ns
$\tau_{-3}$	98.2 ns	126 ns	11 ns
$\tau_{+1}$	7.56 ns	11.30 ns	0.61 ns
$\tau_{+2}$	233 ns	195 ns	7 ns
$\tau_{+3}$	2105 ns	1660 ns	292 ns
$A$	581,754	581,958	7680
$\Theta$	0.5435	9.6167	0.0027
$\eta_{-2}$	0.0153	0.0853	0.0060
$\eta_{-3}$	0.0017	0.0048	0.0012
$\eta_{+2}$	0.0152	0.225	0.015
$\eta_{+3}$	0.0017	0.0519	0.0043

able parametric peak shapes, is the ease to deduce the initial values for the fit parameters. The method to estimate the initial values is shown in Fig. 4. The values of  $\sigma_G$  and  $\mu_G$  can be estimated by fitting a Gaussian to the spectra. The area  $A$  can be estimated from the total counts. The value of  $\Theta$  can be estimated by taking the ratio of counts on the either side of the peak maximum of the spectra. Different  $\tau$  parameters can be estimated by plotting the spectra in log scale and identifying the different linear sections and fitting with exponential functions. The obtained initial guess parameters are listed in Table 4. The fit to the data was performed also using a pure Gaussian function, an Exponential-Gaussian Hybrid function (EGH) [18,36] (see Fig. 2, panels (a) and (b)), a NS-EMG function,

a Dowsett function [15] and a hyper-EMG functions for different tailing orders. To compare the fit results, the goodness of the fit in each case is quantified by calculating the reduced chi-square ( $\chi^2_{red}$ ):

$$\chi^2_{red} = \frac{\chi^2}{\nu}, \quad (17)$$

where  $\nu$ , the degree of freedom, is the number of data points minus the number of fit parameters. An optimal value of the  $\chi^2_{red}$  is close to 1. If the value of  $\chi^2_{red} > 1$ , it indicates that the fit has not properly modeled the data and in the case  $\chi^2_{red} < 1$  the data are overfitted. This condition is based on the assumption that the uncertainties of the bin contents are Gaussian distributed. The  $\chi^2_{red}$  value was calculated for each case and is shown in Fig. 3. The best fit to the data was obtained with the hyper-EMG function with three tails on each side. The high flexibility of hyper-EMG functions to attach independent exponential components to a Gaussian profile enables the good agreement between the data and the fit. The comparison between the hyper-EMG, and other functions shows that the high flexibility is not only necessary to describe the area but also to model accurately the position of the distribution (see Fig. 2b).

The magnified view of the region around the peak maximum of the spectra (see Fig. 2b) shows that a proper modeling of the tails is necessary to describe accurately the data around the peak maximum. The most accurate description of the peak position and the area is obtained with the hyper-EMG. The other fit functions underestimate the peak area, since they do not take the higher order tails into account, which include a significant part of the peak area. This underestimation of the peak area shows up as well in the region of the peak maximum.

The tails observed in Fig. 2 are expected to have the following origin: tails towards longer and shorter flight times can arise from higher-order ion-optical aberrations in the electrostatic mirror system, in the post analyzer reflector and in the extraction channel. The

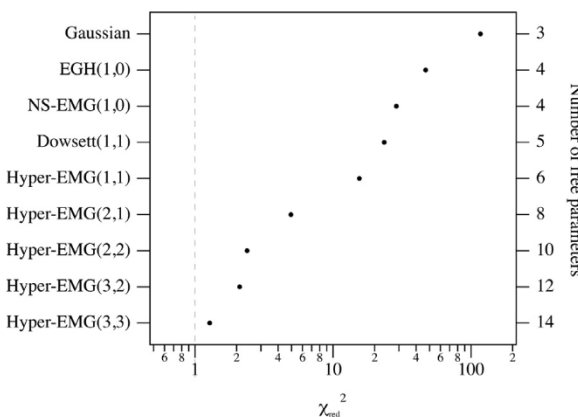
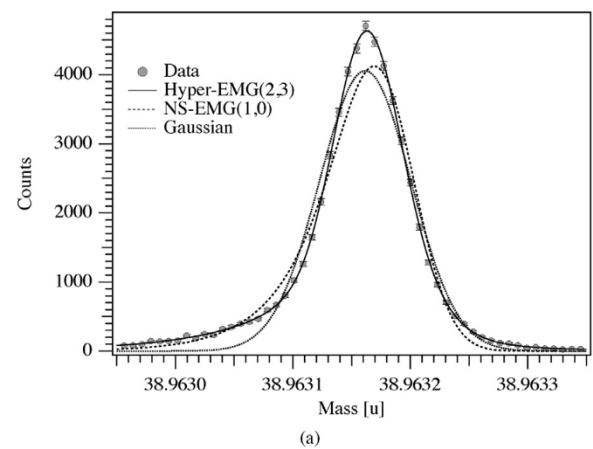


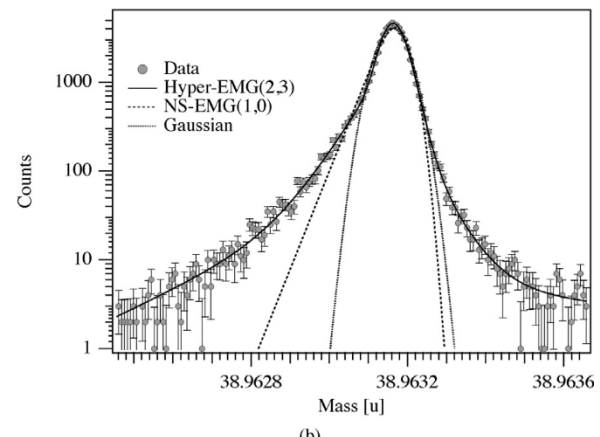
**Fig. 3.** The  $\chi^2_{red}$  value for different models applied to the data in Fig. 2. Here the models used are Gaussian, Exponential-Gaussian Hybrid (EGH) [18], NS-EMG (see Eq. (9)), Dowsett [15], and hyper-EMG (see Eq. (15)). The number of left and right exponential tails included in the function are shown in the brackets, respectively. The total number of free parameters included in the model is shown on the right vertical axis.

dominant contribution of the aberrations belongs to the fourth-order TOF aberration with respect to the energy. This leads to a fourth-order parabola in the time-energy phase space [41]. As a result, a tailing towards longer flight times appears. Further mixed third-order TOF aberrations, which belong to aberrations of second-order in space or angles and first-order in energy, lead to tailing towards both leading and trailing edge of the peak. The tail to the longer flight times belongs to the case that the energy of the ion is smaller than the mean energy of the ions. When the ion energy is larger than the mean energy, the tail appears to shorter flight times. Depending on the experimental conditions the different processes contribute with different strength to the resulting peak shape.

In the previous section, the performance of the hyper-EMG PDF with measured time-of-flight data is demonstrated. The quantitative advantages of a versatile PDF for mass spectrometry can be even more directly shown when it is applied to a converted mass spectrum. In Fig. 5, a measured high-resolution mass spectrum of  $^{39}K^+$  ions from MR-TOF-MS is presented, which is taken from forthcoming publications [40,42]. The spectrum is characterized by a mass resolving power of 520000 related to the FWHM = 70 keV of the distribution. The superb resolving power is obtained after



(a)



(b)

**Fig. 5.** Measured mass spectrum of  $^{39}K^+$  ions from MR-TOF-MS [40]. The achieved mass resolving power is 520,000 at FWHM which corresponds to a width of  $7.49 \times 10^{-5}$  u corresponding to 1.92 ppm (parts-per-million,  $10^{-6}$ ). The number of events in this spectrum is 57455. The mass spectrum is depicted in linear (panel a) and logarithmic (panel b) scales to illustrate the quality of the different fitted curves near the maximum and also in the tails. The filled circles represent the data and the different fitted curves are indicated by the legend.

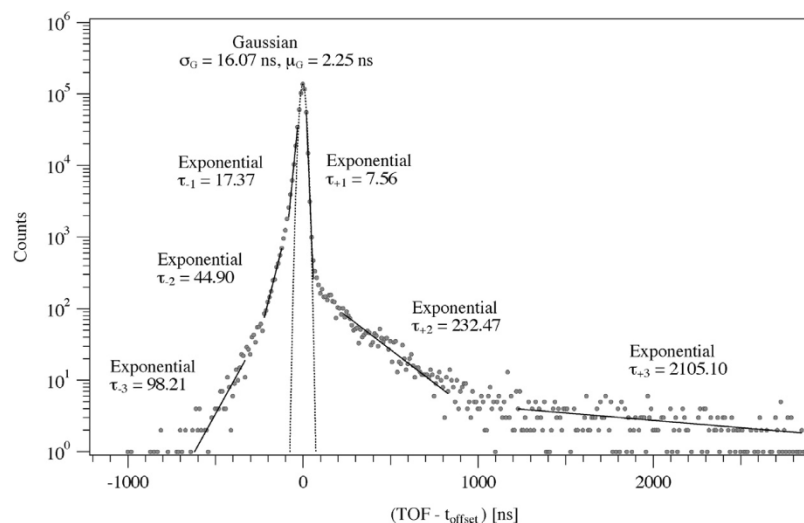


**Fig. 4.** Illustration of the method to assign the initial fit parameters. The different sections of the measured time spectrum from Fig. 2 are modeled with different functions to achieve the initial fit parameters as shown in the figure. The experimental data are represented by grey spheres. The total flight time of this measurement is  $9.9 \times 10^6$  ns which is used as an offset in the presented spectrum.

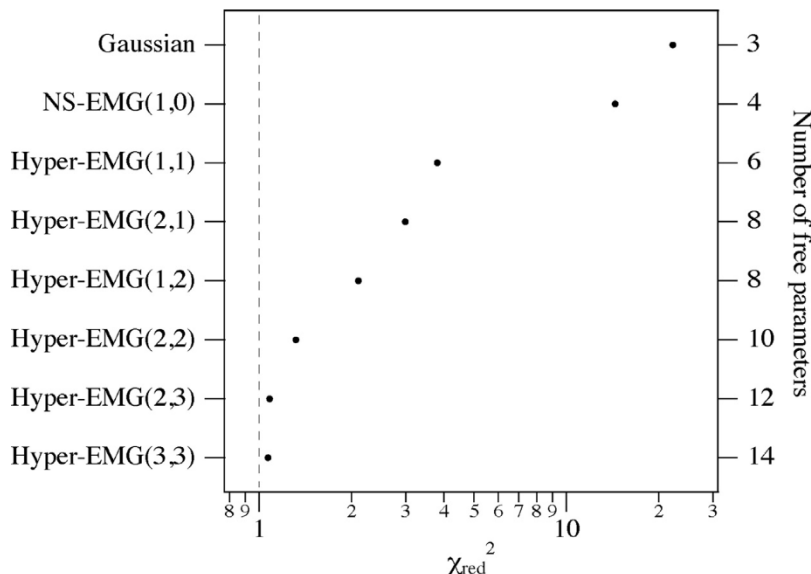


**Fig. 6.** The  $\chi^2_{\text{red}}$  value for different models applied to the data in Fig. 5. Here, the models used are Gaussian, NS-EMG (see Eq. (9)) and hyper-EMG (see Eq. (15)). The number of left and right exponential tails included in the function are indicated in the brackets, respectively. The total number of free parameters included in the models is shown on the right vertical axis.

the ions have traveled 980 laps in the analyzer. This excellent performance has been achieved by many technical improvements as well as the time-correlated data analysis for drift correction. These developments will be described in forthcoming publications [40,42].

A main motivation of this work is to demonstrate the importance of an accurate peak shape model in quantitative analysis of the separated and overlapping mass distributions. From the measured mass distribution of  $^{39}\text{K}^+$  ions two statistically independent distributions with an area ratio of 1:10 is generated by splitting the data. The events in these distributions are 5224 and 52231. These distributions were then positioned exactly at  $2 \times 10^{-3}$  u (1863 keV) and  $0.1 \times 10^{-3}$  u (93.15 keV) mass difference to generate the data for the analysis. For the large distance of  $2 \times 10^{-3}$  u the mass distributions are completely separated, whereas for  $0.1 \times 10^{-3}$  u the distributions overlap. The shift of  $0.1 \times 10^{-3}$  u corresponds 1.33 times the FWHM. The practical results obtained with the hyper-EMG compared with commonly used EMG and Gaussian PDFs are presented. The shifted overlapping mass distributions are presented in Fig. 7. In this simulation based on a measured mass spectrum the true areas and the peak positions are known, i.e., the analysis with the different PDFs gives the uncertainties in mass and abundance determination due to the fit results. This investigation is quite realistic because the shape of the mass distributions is identical for overlapping peaks in high-resolution mass measurements of nuclear physics. In this case, the overlapping peaks represent isobars and isomers. The peak shape conservation can be used to identify unresolved contaminants in the measured mass distribution. The widths of the mass distributions for different isotopes or in general, for species with different masses, are normally different and scale with the mass value under the same experimental conditions during the measurement.

The shape parameters of the distributions were obtained from the high statistic non-overlapping peak (Fig. 5) and were kept constant for the modeling of the overlapping peaks. The free parameters used in the fitting of the overlapping peaks are areas and peak positions corresponding the individual peaks. The fit to the data obtained with different models for single and overlapping peaks are illustrated in Figs. 5 and 7. The errors in the analysis of the peak position for the separated mass spectra are relatively small

( $<3 \times 10^{-3}$  ppm) for all PDFs, even for the case where the data is poorly fitted (see Fig. 6). The striking fact is that only the hyper-EMG reaches the required accuracy for the separated and the overlapping mass distributions with respect to the determination of the area.

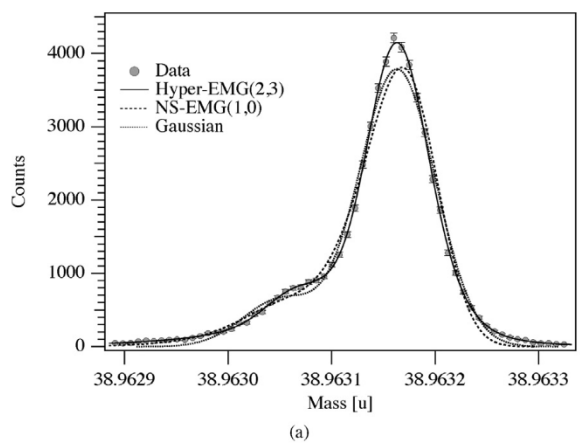
Fig. 8 shows the deviation of the peak position (in keV and ppm) from the true value obtained for different models. The achieved accuracies for the overlapping mass distributions are  $(0.2 \pm 1.2)\%$ ,  $(28 \pm 1)\%$ ,  $(12.5 \pm 0.8)\%$  deviations from the known distance of 93.15 keV for the hyper-EMG(2,3), the NS-EMG and the Gaussian, respectively (see Fig. 8).

Fig. 9 shows the deviation of the individual peak areas and area ratio from the true value obtained for different models. Here the hyper-EMG reproduce the true value by an order of magnitude better than other commonly used models even in the case of area ratio where one expect the tailing effects would cancel.

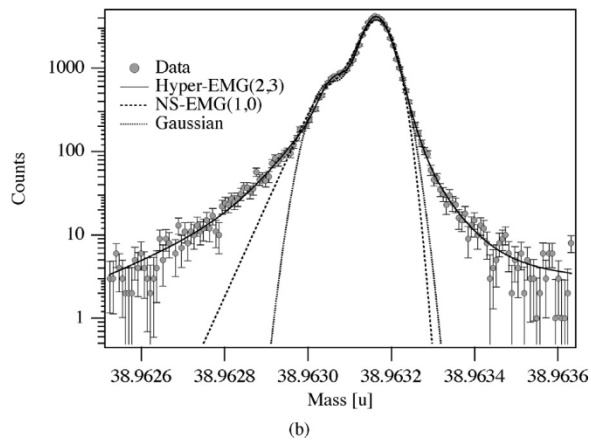
Hyper-EMG (2,3) is the optimal choice for this particular case since this function reproduce the peak shift (see Fig. 8), true areas (see Fig. 9a) and the true ratio of the areas (see Fig. 9b) within the statistical uncertainties with the minimum number of parameters. Figs. 8 and 9 shows that the EMG and Gaussian PDFs clearly failed to reproduced the results within the statistical uncertainty. The conclusion is that only the hyper-EMG is well suited for accurate mass analysis to evaluate the overlapping distributions, e.g., mixtures of ground state and low-excited nuclei.

## 6. Summary and outlook

In this work, a new analytical probability distribution function, the hyper-EMG, is developed. It is capable of modeling measured distributions with a central Gaussian part with either one or both of its sides modified by multiple exponentials of different strengths. The hyper-EMG is obtained by the convolution of a Gaussian distribution with hyper-exponential functions decreasing towards both positive and negative directions. The application of the hyper-EMG in modeling MR-TOF-MS spectra has been quantitatively demonstrated. The hyper-EMG has been applied to high-resolution experimental time and mass spectra characterized by mass resolving powers of 140,000 and 520,000 obtained with  $^{133}\text{Cs}^+$  and  $^{39}\text{K}^+$  ions, respectively. From the measured mass distribution of  $^{39}\text{K}^+$



(a)



(b)

**Fig. 7.** Simulated overlapping mass spectra deduced from the measured mass spectrum of  $^{39}\text{K}^+$  ions [40]. Two statistical independent distributions are generated from the measured distribution (see Fig. 5) with an exact intensity ratio of 1:10 and a peak distance of  $0.1 \times 10^{-3}$  u corresponding to 93.15 keV and 2.6 ppm. The peak positions and the areas are thus known and represent ideal tests for the performance of the different PDFs. The overlapped distributions have identical shapes with a FWHM of 70 keV. The mass spectrum is depicted in linear (panel a) and logarithmic (panel b) scales to illustrate the quality of the different fitted curves near the maximum and in the tails. The filled circles represent the data. The different fitted curves are explained by the legend.

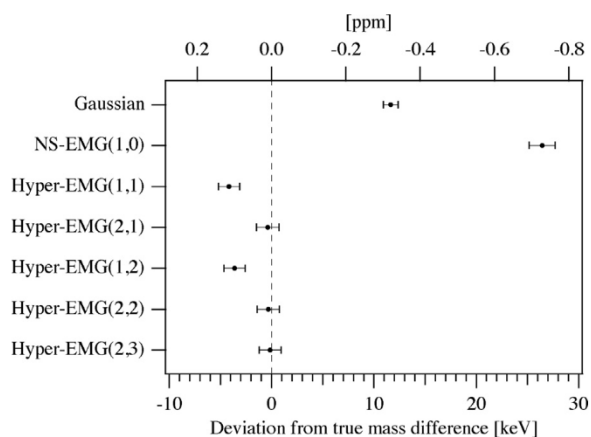
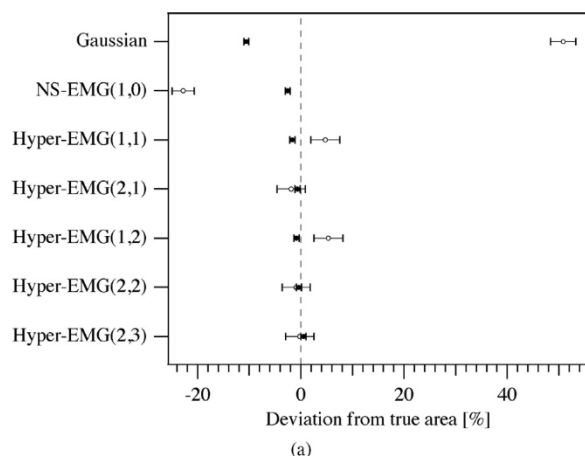
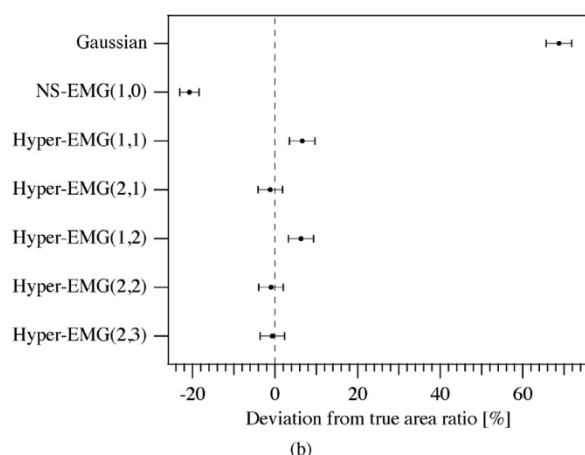


**Fig. 8.** Determined position differences for the overlapping mass distributions. The peaks are accurately positioned at a distance of  $0.1 \times 10^{-3}$  u corresponding to 93.15 keV and 2.6 ppm and thus overlap. The peak differences obtained with different fit functions are compared with the true value. The number of left and right exponential tails included in the fit function are indicated in the brackets, respectively.



(a)



(b)

**Fig. 9.** Determined areas for the overlapped mass distributions with different PDFs. In panel (a) the relative deviations from true areas of the high (closed circles) and low-intensity (open circles) peaks are given. In panel (b) the ratios of the areas of the overlapped peaks are determined with different fit functions and compared with the true value. The number of left and right exponential tails included in the function is shown in the brackets, respectively.

ions two overlapping, statistically independent distributions with a peak difference of 2.6 ppm and an area ratio of 1:10 are generated and analyzed. With the superb resolving power of  $^{39}\text{K}^+$  ions an accuracy of  $(0.2 \pm 1.2)\%$  for the absolute peak difference and  $(0.5 \pm 0.5)\%$  (large peak) and  $(0.2 \pm 2.7)\%$  (small peak) for the absolute peak areas has been achieved, respectively. The ratio of the areas of the overlapped distributions were reproduced with an accuracy of  $(1 \pm 3)\%$ . The results reveal significant advantages of the new PDF for the evaluation of overlapping distributions. The accurate peak and area determinations compared with commonly used PDFs are more than an order of magnitude more accurate. With the obtained resolving power of 520,000 in this mass range the obtained accuracy represents a unique experimental tool for the research with exotic nuclei which is complementary to the traditional photon spectroscopy. Of course, one has to take into account that for rare exotic nuclei the intensities are much lower in on-line experiments, because the production cross sections of interesting nuclides are very small [1].

The developed hyper-EMG will be used for the analysis of recently measured new masses of  $^{238}\text{U}$  projectile and fission fragments and also for the experimental study of mass-resolved isomers [43,44,40]. The experiments have been performed with the FRS Ion Catcher facility [35] which includes the fragment separator FRS [45] and the cryogenic stopping cell [46].

High-resolution time-of-flight mass spectrometers can be used also in other fields [47]. Mobile and compact MR-TOF-MS can be used in chromatographic, medical, biological and environmental applications. Moreover, the MR-TOF-MS are now commercially available for analytical mass spectrometry which can also open new fields [48,49]. In all of these fields the presented hyper-EMG can be well applied to analyze the measured spectra. In addition, the hyper-EMG can also be used in modeling data from photon detectors or measured energy-loss distributions of heavy ions penetrating through matter [50].

## Acknowledgments

This work was supported by the German Federal Ministry for Education and Research (BMBF) under contract no. 05P12RGFN8, by the Hessian Ministry for Science and Art (HMWK) through the LOEWE Center HICforFAIR, by HGS-HIRE, and by Justus-Liebig-Universität Gießen and GSI under the JLU-GSI strategic Helmholtz partnership agreement.

## References

- [1] H. Geissel, M. Huyse, G. Münzenberg, P. Van Duppen, Exotic Nuclear Beam Facilities, Wiley Online Library, 2014.
- [2] H. Grawe, K. Langanke, G. Martínez-Pinedo, Nuclear structure and astrophysics, *Rep. Prog. Phys.* 70 (9) (2007) 1525.
- [3] R. Wolf, F. Wienholtz, D. Atanasov, D. Beck, K. Blaum, C. Borgmann, F. Herfurth, M. Kowalska, S. Kreim, Y.A. Litvinov, et al., Isoltrap's multi-reflection time-of-flight mass separator/spectrometer, *Int. J. Mass Spectrom.* 349 (2013) 123–133.
- [4] W.R. Plaß, T. Dickel, C. Scheidenberger, Multiple-reflection time-of-flight mass spectrometry, *Int. J. Mass Spectrom.* 349 (2013) 134–144.
- [5] F. Wienholtz, D. Beck, K. Blaum, C. Borgmann, M. Breitenfeldt, R.B. Cakirli, S. George, F. Herfurth, J. Holt, M. Kowalska, et al., Masses of exotic calcium isotopes pin down nuclear forces, *Nature* 498 (7454) (2013) 346.
- [6] T. Dickel, W. Plaß, S.A. San Andres, J. Ebert, H. Geissel, E. Haettner, C. Hornung, I. Miskun, S. Pietri, S. Purushothaman, et al., First spatial separation of a heavy ion isomeric beam with a multiple-reflection time-of-flight mass spectrometer, *Phys. Lett. B* 744 (2015) 137–141.
- [7] P. Schury, M. Wada, Y. Ito, D. Kaji, F. Arai, M. MacCormick, I. Murray, H. Haba, S. Jeong, S. Kimura, et al., First online multireflection time-of-flight mass measurements of isobar chains produced by fusion-evaporation reactions: Toward identification of superheavy elements via mass spectroscopy, *Phys. Rev. C* 95 (1) (2017) 011305.
- [8] P.M. Walker, Isomer building blocks and k-forbidden decays, *Phys. Scr.* 92 (5) (2017) 054001.
- [9] J. Routti, S. Prussin, Photopeak method for the computer analysis of gamma-ray spectra from semiconductor detectors, *Nucl. Instrum. Methods* 72 (2) (1969) 125–142.
- [10] I.G. McWilliam, H.C. Bolton, Instrumental peak distortion. I. Relaxation time effects, *Anal. Chemistry* 41 (13) (1969) 1755–1762.
- [11] R. Fraser, T. MacRae, E. Suzuki, Chain conformation in the collagen molecule, *J. Mol. Biol.* 129 (3) (1979) 463–481.
- [12] R. Delley, Modifying the Gaussian peak shape with more than one time constant, *Anal. Chem.* 58 (11) (1986) 2344–2346.
- [13] G. Bortels, P. Collaers, Analytical function for fitting peaks in alpha-particle spectra from Si detectors, *Int. J. Radiat. Appl. Instrum. Part A. Appl. Radiat. Isot.* 38 (10) (1987) 831–837.
- [14] A. Berthod, Mathematical series for signal modeling using exponentially modified functions, *Anal. Chem.* 63 (17) (1991) 1879–1884.
- [15] M. Dowsett, G. Rowlands, P. Allen, R. Barlow, An analytic form for the SIMS response function measured from ultra-thin impurity layers, *Surf. Interface Anal.* 21 (5) (1994) 310–315.
- [16] J. Li, Development and evaluation of flexible empirical peak functions for processing chromatographic peaks, *Anal. Chem.* 69 (21) (1997) 4452–4462.
- [17] A. Felinger, Data Analysis and Signal Processing in Chromatography, vol. 21, Elsevier, 1998.
- [18] K. Lan, J.W. Jorgenson, A hybrid of exponential and Gaussian functions as a simple model of asymmetric chromatographic peaks, *J. Chromatogr. A* 915 (1) (2001) 1–13.
- [19] V.B. Di Marco, G.G. Bombi, Mathematical functions for the representation of chromatographic peaks, *J. Chromatogr. A* 931 (1) (2001) 1–30.
- [20] J. Li, Comparison of the capability of peak functions in describing real chromatographic peaks, *J. Chromatogr. A* 952 (1) (2002) 63–70.
- [21] W. Feller, An Introduction to Probability Theory and Its Applications, vol. 1, 3rd ed., John Wiley & Sons London-New York-Sydney-Toronto, 1968.
- [22] F. James, Statistical Methods in Experimental Physics, World Scientific, 2006.
- [23] S. Frühwirth-Schnatter, Finite Mixture and Markov Switching Models, Springer Science & Business Media, 2006.
- [24] C. Chatfield, C. Theobald, Mixtures and random sums, in: *The Statistician*, 1973, pp. 281–287.
- [25] B.S. Everitt, An introduction to finite mixture distributions, *Stat. Methods Med. Res.* 5 (2) (1996) 107–127.
- [26] Ü Erişoğlu, M. Erişoğlu, H. Erol, A mixture model of two different distributions approach to the analysis of heterogeneous survival data, *Int. J. Comput. Math. Sci.* 5 (2) (2011).
- [27] N.P. Jewell, Mixtures of exponential distributions, *Ann. Stat.* (1982) 479–484.
- [28] T.-H. Kim, H. White, On more robust estimation of skewness and kurtosis, *Finance Res. Lett.* 1 (1) (2004) 56–73.
- [29] E. Grushka, Characterization of exponentially modified Gaussian peaks in chromatography, *Anal. Chem.* 44 (11) (1972) 1733–1738.
- [30] M. Guilhaus, Special feature: tutorial. Principles and instrumentation in time-of-flight mass spectrometry. Physical and instrumental concepts, *J. Mass Spectrom.* 30 (11) (1995) 1519–1532.
- [31] H. Wollnik, Mass separators, *Nucl. Instrum. Methods Phys. Res. Sect. A: Accel. Spectrom. Detect. Assoc. Equip.* 258 (3) (1987) 289–296.
- [32] A. Casares, A. Kholomeev, H. Wollnik, Multipass time-of-flight mass spectrometers with high resolving powers, *Int. J. Mass Spectrom.* 206 (3) (2001) 267–273.
- [33] Y. Ishida, M. Wada, H. Wollnik, A multi-reflection time-of-flight mass spectrometer for mass measurements of short-lived nuclei, *Nucl. Instrum. Methods Phys. Res. Sect. B: Beam Interact. Mater. Atoms* 241 (1) (2005) 983–985.
- [34] T. Dickel, W. Plaß, A. Becker, U. Czok, H. Geissel, E. Haettner, C. Jesch, W. Kinsel, M. Petrick, C. Scheidenberger, et al., A high-performance multiple-reflection time-of-flight mass spectrometer and isobar separator for the research with exotic nuclei, *Nucl. Instrum. Methods Phys. Res. Sect. A: Accel. Spectrom. Detect. Assoc. Equip.* 777 (2015) 172–188.
- [35] W. Plaß, T. Dickel, S. Purushothaman, P. Dendooven, H. Geissel, J. Ebert, E. Haettner, C. Jesch, M. Ranjan, M. Reiter, et al., The FRS ion catcher – A facility for high-precision experiments with stopped projectile and fission fragments, *Nucl. Instrum. Methods Phys. Res. Sect. B: Beam Interact. Mater. Atoms* 317 (2013) 457–462.
- [36] P. Schury, M. Wada, Y. Ito, F. Arai, S. Naimi, T. Sonoda, H. Wollnik, V. Shchepunov, C. Smorra, C. Yuan, A high-resolution multi-reflection time-of-flight mass spectrograph for precision mass measurements at RIKEN/SLOWRI, *Nucl. Instrum. Methods Phys. Res. Sect. B: Beam Interact. Mater. Atoms* 335 (2014) 39–53.
- [37] W.A. Wheaton, A.L. Dunklee, A.S. Jacobsen, J.C. Ling, W.A. Mahoney, R.G. Radocinski, Multiparameter linear least-squares fitting to poisson data one count at a time, *Astrophys. J.* 438 (1995) 322–340.
- [38] J.W. Fowler, Maximum-likelihood fits to histograms for improved parameter estimation, *J. Low Temp. Phys.* 176 (3–4) (2014) 414–420.
- [39] S. Baker, R.D. Cousins, Clarification of the use of chi-square and likelihood functions in fits to histograms, *Nucl. Instrum. Methods Phys. Res.* 221 (2) (1984) 437–442.
- [40] S. Ayet San Andrés, Doctoral Thesis in Preparation, Universität Gießen, 2017.
- [41] M.I. Yavor, W.R. Plaß, T. Dickel, H. Geissel, C. Scheidenberger, Ion-optical design of a high-performance multiple-reflection time-of-flight mass spectrometer and isobar separator, *Int. J. Mass Spectrom.* 381 (2015) 1–9.
- [42] S. Ayet San Andrés et al., manuscript in preparation.
- [43] J. Ebert, Mass Measurements of  $^{238}\text{U}$ -Projectile Fragments for the First Time With a Multiple-Reflection Time-Of-Flight Mass Spectrometer, Universität Gießen, 2016, Ph.D. Thesis.
- [44] C. Hornung, Doctoral thesis in preparation, Universität Gießen, 2017.
- [45] H. Geissel, P. Armbruster, K.H. Behr, A. Brünle, K. Burkard, M. Chen, H. Folger, B. Franzak, H. Keller, O. Klepper, et al., The GSI projectile fragment separator (FRS): a versatile magnetic system for relativistic heavy ions, *Nucl. Instrum. Methods Phys. Res. Sect. B: Beam Interact. Mater. Atoms* 70 (1–4) (1992) 286–297.
- [46] S. Purushothaman, M. Reiter, E. Haettner, P. Dendooven, T. Dickel, H. Geissel, J. Ebert, C. Jesch, W. Plass, M. Ranjan, et al., First experimental results of a cryogenic stopping cell with short-lived, heavy uranium fragments produced at 1000 MeV/u, *EPL (Europhys. Lett.)* 104 (4) (2013) 42001.
- [47] T. Dickel, W. Plaß, J. Lang, J. Ebert, H. Geissel, E. Haettner, C. Jesch, W. Lippert, M. Petrick, C. Scheidenberger, et al., Multiple-reflection time-of-flight mass spectrometry for in situ applications, *Nucl. Instrum. Methods Phys. Res. Sect. B: Beam Interact. Mater. Atoms* 317 (2013) 779–784.
- [48] C.F. Klitzke, Y.E. Corilo, K. Siek, J. Binkley, J. Patrick, M.N. Eberlin, Petroleomics by ultrahigh-resolution time-of-flight mass spectrometry, *Energy Fuels* 26 (9) (2012) 5787–5794.
- [49] G.A. Bataglion, C.F. Klitzke, A.C.R. de Albergaria-Barbosa, M. Frena, L.A. dos Santos Madureira, R.R. Weber, M.C. Bícego, M.N. Eberlin, Fatty acid biomarkers in sediment samples via ultra-high resolution and accuracy time-of-flight mass spectrometry, *Org. Geochem.* 92 (2016) 24–31.
- [50] H. Geissel, H. Weick, C. Scheidenberger, R. Bimbot, D. Gardes, Experimental studies of heavy-ion slowing down in matter, *Nucl. Instrum. Methods Phys. Res. Sect. B: Beam Interact. Mater. Atoms* 195 (1) (2002) 3–54.